energies

MDPI

Article

Wave Energy Converter Feasibility in Türkiye's Surrounding Waters: A Twenty-Year, Four-Basin Assessment

Ahmet Durap

Engineering and Natural Sciences Faculty, Istanbul Medipol University, 34181 Istanbul, Türkiye; ahmetdurap@gmail.com or ahmet.durap@medipol.edu.tr

Abstract

Wave energy in short-fetch, semi-enclosed seas depends on how closely the response of a converter matches locally generated, short-period waves. This study makes that match explicit for the Black Sea, the Sea of Marmara, the Aegean, and the Eastern Mediterranean, the four seas around Türkiye, as four distinct regions within a single study area. Twenty years (May 2006 to March 2026) of three-hourly significant wave height and energy period from the Copernicus Marine global wave reanalysis (0.2°) were combined with GEBCO 2026 bathymetry to map the wave power flux, to screen cells inside a first-order 25–100 m deployment-depth band, and to rank three candidate sites in each region. Specific power matrices were applied to three full-scale reference converters (Pelamis P-750, AquaBuOY and Wave Dragon) and to two shallow-water archetypes, the Oyster surge flap and the Wavestar multi-float machine, standing for contemporary shallow-water design classes, at full scale and under Froude similitude. The best deployable sites of the Black Sea and the Aegean carry mean fluxes of 3.1–3.6 kW m^{-1}, and the Marmara sites define the low-resource end member at 0.2–0.8 kW m^{-1}; mean energy periods at the twelve sites range from 2.7 to 5.4 s. At their original scale the three reference converters reach capacity factors of up to 3.4%, because their specific power matrix response bands fall largely outside the regional sea-state distribution. Scaling changes that. Froude scaling to 0.20–0.25 of the original linear dimensions moves the response into the dominant 4–5 s band and raises the capacity factor to 30–47% at the seven sites where the mean flux exceeds 2.5 kW m^{-1}, at scaled rated powers of about 2–25 kW; the two archetypes reach 7–19% at full scale and 49–59% once scaled at the same sites. Both the preferred scale and the achievable capacity factor are near-uniform along the Black Sea rim, the Aegean archipelago, and the Levantine shore, so the analysis yields a single regional design specification, as follows: a small, short-period converter deployed in modular arrays.

Keywords: wave energy; wave energy converter; capacity factor; power matrix; Black Sea; Sea of Marmara; Aegean Sea; Eastern Mediterranean; Copernicus Marine reanalysis; Froude scaling; site selection

Academic Editors: Lars Johanning and Yongliang Zhang

Received: 1 July 2026
Revised: 18 August 2026
Accepted: 19 August 2026
Published: 20 August 2026

1. Introduction

Ocean waves carry one of the largest untapped renewable resources on the planet, with a global theoretical potential of roughly two terawatts concentrated where long Atlantic and Southern Ocean swells meet the western coasts of the continents [1,2]. Most early device development followed that resource, so the leading wave energy converters were sized for seas with energy periods of eight seconds or more and wave heights of several metres. The enclosed and semi-enclosed seas of southern Europe received comparatively little device-level attention. That has changed over the past decade. Their waves are smaller, but they are also shorter, closer to shore, and less violent, which lowers survival loads and shortens transmission distances. Coastal demand in these regions is high and largely met by imported fuel, so even a modest local resource is worth quantifying carefully [3,4].

Türkiye is a useful test case. Water borders the country on three sides, as follows: the Aegean and the Eastern Mediterranean to the west and south, the Sea of Marmara between them, and the Black Sea to the north. The coastline runs to more than 8000 km and folds into bays, straits, and exposed capes where local winds build steep seas. Hindcast studies of the Black Sea have put the mean wave power at about 3 to 6 kW m^{-1} along its western and south-western edges [5,6], and work in the Aegean has pointed to the central archipelago, where the summer Etesian (meltemi) winds drive a steady northerly sea [7]. What is still missing is the next step. Knowing the resource is not the same as knowing what a converter would actually produce in it, and very few studies have closed that gap for Turkish waters.

The output of a wave energy converter depends on how often the local sea states fall inside the device power matrix, the table of electrical output across the wave heights, and periods that excite the device, which folds together its hydrodynamic response and the conversion efficiency of its power take-off [8]. Devices such as the Pelamis attenuator, the AquaBuOY point absorber, and the Wave Dragon overtopping terminator reach rated power only when the period is roughly 7 to 11 s and the wave height is several metres [9]. In the Mediterranean and the Black Sea, the sea is dominated by locally generated wind waves with energy periods that seldom pass 5 to 6 s, so these machines operate below cut-in for most of the year. Bozzi et al. [3] quantified the consequence across the whole Mediterranean, as follows: full-scale converters returned capacity factors of 4 to 9%, but shrinking the devices under Froude similitude, so that their natural response matched the shorter local waves, lifted the capacity factor above 30%. Site studies at Menorca [10] and off Lebanon [11] reached the same conclusion from different data.

This paper extends that line of work to the four seas around Türkiye, extending the approach to a domain that earlier basin studies did not cover. Three elements are new. First, the Black Sea and the Sea of Marmara are brought into a device-level assessment alongside the Aegean and the Eastern Mediterranean, with three candidate sites in each of the four regions, so that no basin is represented by a single point; to the author's knowledge, the Marmara has not previously appeared in a converter performance study at all. Second, the site screen is made consistent with the machines, as follows: candidate cells are restricted to the 25–100 m depth band in which the reference devices are actually designed to operate, so the sites are places where a device could plausibly be moored. Third, the analysis is carried along the entire coastline of the domain, not only at the ranked sites, so the Froude-scaling result is presented as coast-wide maps of the achievable capacity factor and of the optimal device scale. Section 2 describes the data, the regional division, the converters, and their specific power matrices, and the methods. Section 3 reports the resource and the device performance. Section 4 sets the numbers against the literature, discusses the practical implications of arrays of small devices, and notes the limits of the method. Section 5 draws the work together.

2. Materials and Methods

2.1. Study Area and Regional Division

The domain runs from 24.4° to 45.0° E and from 33.8° to 48.4° N and is divided into four regions that meet at the Turkish Straits (Figure 1). The Black Sea is almost closed, so its waves are built entirely by local winds and the resource gathers in the western and central interior. The Sea of Marmara is a small, fetch-limited basin between the Bosphorus and the Dardanelles; it is included here because it has essentially never been examined in a device-level wave energy study, and because its sheltered water is exactly where small-scale technology would first be tested. The Aegean is deep and broken by islands; it sees northerly Etesian winds in summer and travelling depressions in winter. The Eastern Mediterranean, or Levantine, basin carries the strongest deep-water waves in the domain, although the energetic water lies well offshore. Each 0.2° grid cell of the wave reanalysis is assigned to one region by the simple geographic rules drawn in Figure 1b, and Table 1 summarises the four regions. The division is analytic, so it can be reproduced exactly.

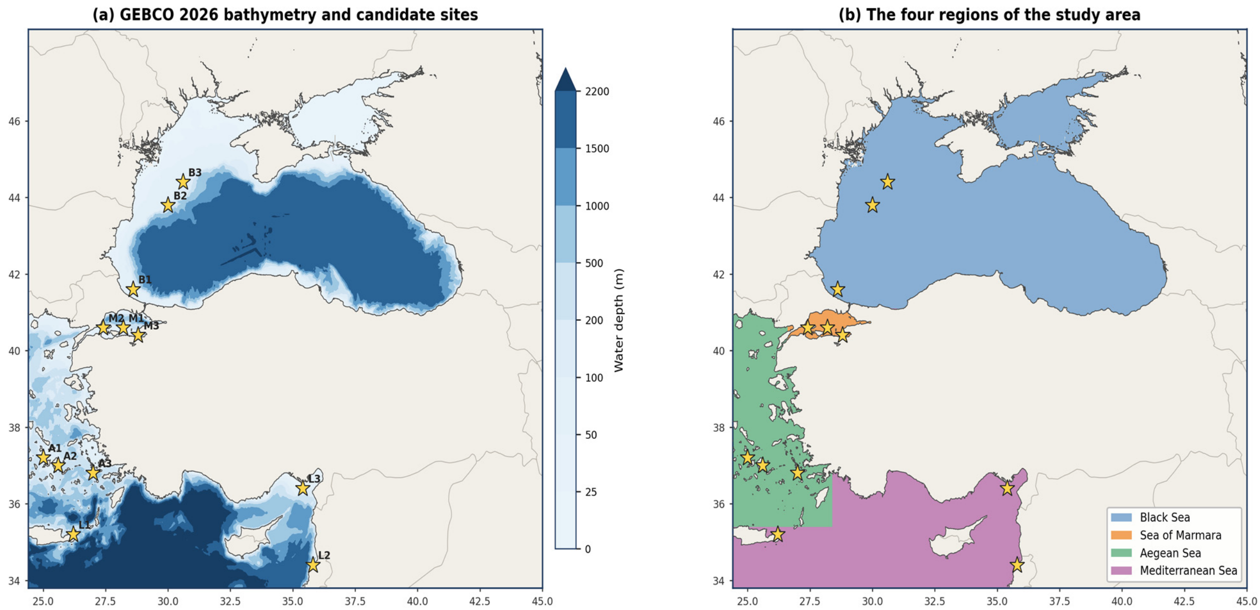

Figure 1. Study area. (**a**) GEBCO 2026 bathymetry with the twelve candidate sites. (**b**) Assignment of the sea to the four regions: Black Sea, Sea of Marmara, Aegean Sea, and Mediterranean Sea. Coastlines are drawn from the GEBCO 2026 grid; thin grey lines are national borders (B stands for Black Sea, M for Marmara, A for Aegean, L for Levantine, namely Mediterranean).

Table 1. The four regions: number of valid 0.2° sea cells, number of deployable cells (25–100 m), and twenty-year regional means of the wave power flux P, significant wave height H_{m0}, and energy period T_e.

Region	Sea Cells	Deployable Cells	P (kW m^{-1})	H_{m0} (m)	T_e (s)	Max P (kW m^{-1})
Black Sea	1312	196	2.41	0.74	4.23	3.77
Marmara	37	17	0.45	0.33	2.79	0.86
Aegean	420	78	2.69	0.81	4.16	4.74
Mediterranean	660	22	3.45	0.87	4.95	6.47

2.2. Wave Reanalysis Data

Sea states were taken from the Copernicus Marine Environment Monitoring Service global ocean wave reanalysis WAVERYS (product cmems_mod_glo_wav_my) at 0.2° resolution and three-hourly output; at 38° N a 0.2° cell spans about 22 km meridionally and 17 km zonally. The product is built on the MFWAM spectral wave model, forced by ERA5 winds and constrained by assimilation of along-track altimeter wave height [12]. At this resolution, the larger Aegean islands are resolved as land cells, but islands smaller than a cell are not represented individually, so wave sheltering inside the archipelago is captured only partly; what this means for the numbers is taken up in Section 4. Two fields were read for every time step, as follows: the spectral significant wave height H_{m0} (variable VHM0) and the energy period T_e (variable VTM10, the $T_{m-1,0}$ moment period). After concatenation, the archive held 57,982 three-hourly fields from 28 May 2006 to 31 March 2026, that is 19.9 years, on a 74 × 104 grid. Cells that returned valid data over the whole period define the sea mask used throughout; the Sea of Marmara is resolved by 37 fully valid cells, which is coarse but sufficient for the basin-scale statements made here.

One point about consistency deserves care. Basins do not need to be simulated by one model to be comparable, and regional models tuned to individual seas are often more accurate locally. What a fair cross-basin comparison does require is that the input variables carry the same definition and provenance in every basin, as follows: the same pair (H_{m0}, T_e), produced by the same physics, the same forcing, and the same record length, so that a difference between two sites reflects the sea and not the dataset. A single reanalysis is a convenient way to guarantee this, and the coarse 0.2° resolution it imposes is the price, revisited in Section 4.

2.3. Bathymetry

Water depth came from the GEBCO 2026 grid at 15 arc-second resolution [13] rather than from the wave model itself. The model carries one depth per 0.2° cell, which is adequate for wave propagation but says nothing about the depth structure inside a 20 km cell, and that structure is exactly what a mooring screen needs. The GEBCO grid was therefore averaged onto each wave cell using only submerged pixels, so partially-land cells are not biased by dry ground, to give one representative depth per cell; this feeds the maps in Section 3 and the depth screen in Section 2.6. The same grid supplies the coastlines of every map in the paper.

2.4. Wave Power and Sea-State Descriptors

The wave energy flux, the power crossing a vertical plane one metre wide per unit crest length, follows from the directional wave spectrum $S(f, \theta)$ as

$$P = \rho g \iint c_g(f, d)\, S(f, \theta)\, df\, d\theta, \tag{1}$$

where ρ is the sea-water density, g the gravitational acceleration, and c_g the group velocity, which depends on frequency f and water depth d. In deep water, the group velocity reduces to $c_g = gT/4\pi$, and Equation (1) collapses to the compact form used here,

$$P = (\rho g^2/64\pi)\, H_{m0}{}^2\, T_e, \tag{2}$$

with $\rho = 1025$ kg m^{-3} and $g = 9.81$ m s^{-2}; P is reported in kW m^{-1}. The two descriptors in Equation (2) are themselves spectral moments, $m_n = \int f^n S(f)\, df$, through

$$H_{m0} = 4\sqrt{m_0}, \qquad T_e = m_{-1}/m_0. \tag{3}$$

Equation (2) assumes deep water, which holds at the candidate sites (depths of 58 m or more, Section 3.3) for the dominant periods. The time-mean, monthly-mean, and seasonal-mean flux were accumulated cell by cell across all 57,982 steps, together with the mean H_{m0} and T_e and the full joint histogram of (H_{m0}, T_e) in bins of 0.25 m by 0.25 s, which Section 2.8 turns into device output.

2.5. Resource Variability Metrics

How evenly the resource is spread through the year bears on predictability, storage sizing, and grid integration, so two standard descriptors were computed at each site.

The seasonal variability index compares the strongest and weakest monthly means against the annual mean,

$$\mathrm{SV} = (P_{\mathrm{M,max}} - P_{\mathrm{M,min}})/P_{\mathrm{year}}, \tag{4}$$

where $P_{\mathrm{M,max}}$ and $P_{\mathrm{M,min}}$ are the highest and lowest monthly-mean flux and P_{year} the annual mean [14]. The temporal coefficient of variation COV, the standard deviation of the three-hourly flux divided by its mean, captures the shorter-term spikiness that drives loads and storage needs. Interannual behaviour was taken from the complete calendar years 2007–2025 and summarised by the standard deviation of the annual-mean flux and by an ordinary least-squares trend fitted to it.

2.6. Site Selection

Candidate sites had to be places a device could actually occupy. Cells were kept only if they carried a valid resource and had a representative depth between 25 and 100 m. That interval was adopted as a first-order screening band spanning portions of the documented deployment-depth ranges of the three reference concepts in Table 2, as follows: the floating Pelamis and AquaBuOY are moored in roughly 50–150 m, while the Wave Dragon is designed for 25–40 m. The band is therefore wider than the depths common to all three, and it is tied to the device envelopes of Table 2 rather than chosen for the resource. Within the deployable set of each region the cells were ranked by mean flux, and the best three were taken under the rule that no two sites lie within 0.6° of each other, so the selection samples distinct stretches of coast in every basin instead of clustering on a single peak. The result is twelve sites, three per region (Section 3.3).

2.7. Wave Energy Converters and Power Matrices

Three converters were chosen to span the main working principles rather than to favour any one design, as follows [15]: the Pelamis P-750 attenuator, the AquaBuOY point absorber, and the Wave Dragon overtopping terminator. Pelamis Wave Power ceased trading in 2014, and Pelamis and AquaBuOY are treated here as legacy reference technologies; all three devices enter the analysis as specific power matrix benchmarks available for scaling rather than as procurement-ready products. Figure 2 sketches the three working principles and Table 2 lists the principal characteristics. Each device is described by its specific power matrix $p(H_{\mathrm{m0}}, T)$, the electrical output across bins of wave height and period. The matrix is the appropriate description for a resource study because it already contains the physics the devices differ in, as follows: the hydrodynamic response of the hull to each combination of height and period, and the conversion efficiency of the power take-off, appear jointly as the ratio of the tabulated electrical output to the incident wave power in the corresponding bin. The three matrices are reproduced in full in Appendix A (Tables A1–A3), exactly as given by Silva et al. [16], so every device number in this paper can be recomputed from the printed tables.

The Pelamis P-750 [17] is a 150 m long, 3.5 m diameter attenuator rated at 750 kW; its matrix is binned in energy period T_{e} from 5 to 13 s. The AquaBuOY [18] is a 6 m diameter heaving buoy rated at 250 kW, and the Wave Dragon [19] a 300 m wide overtopping platform rated at 7 MW; their matrices are binned in peak period T_{p} from 5 to 17 s. Where a matrix is binned in T_{p}, the reanalysis energy period is converted with the standard JONSWAP-spectrum relation $T_{\mathrm{p}} \approx T_{\mathrm{e}}/0.9$ [16]. The three devices differ most in the period band over which they respond (Table 2), and that difference drives the results in Section 3.4.

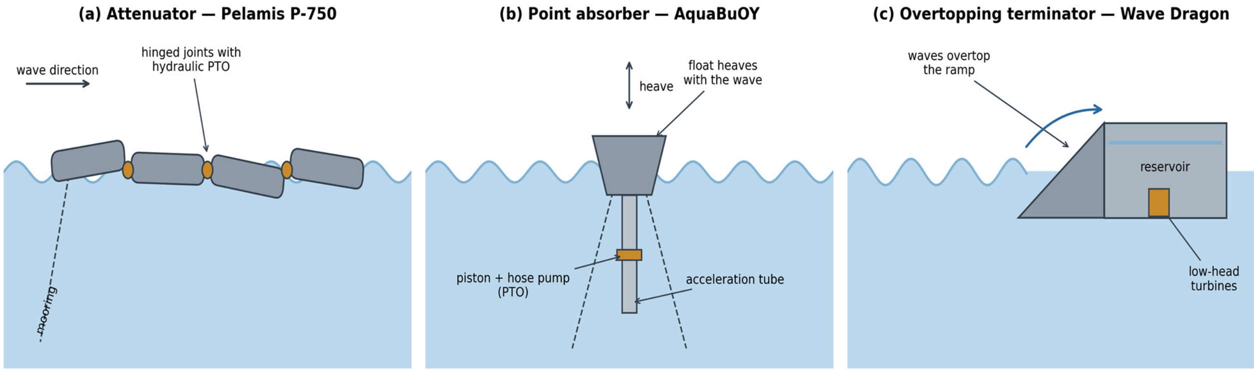

Figure 2. Working principles of the three reference converters. (**a**) The Pelamis attenuator: articulated cylinders aligned with the wave direction flex at hinged joints whose hydraulic rams pump fluid through motors. (**b**) The AquaBuOY point absorber: a float heaves against a submerged acceleration tube; a piston and hose pump form the power take-off. (**c**) The Wave Dragon terminator: waves run up a ramp and overtop into a floating reservoir that drains through low-head turbines.

Table 2. Reference converters: working principle, rated power, characteristic dimensions, design operating depth, and the axes of the specific power matrices (Appendix A).

Device	Principle	Rated Power	Dimensions	Depth (m)	Matrix Axes	Ref.
Pelamis P-750	Attenuator	750 kW	L 150 m, Ø 3.5 m	50–150	$H_{\mathrm{m0}} \times T_{\mathrm{e}}$	[17]
AquaBuOY	Point absorber	250 kW	Ø 6 m, tube 30 m	≥50	$H_{\mathrm{m0}} \times T_{\mathrm{p}}$	[18]
Wave Dragon	Overtopping terminator	7000 kW	width 300 m	25–40	$H_{\mathrm{m0}} \times T_{\mathrm{p}}$	[19]

No manufacturer power matrix is public for the contemporary shallow-water devices, so two further specific power matrices are used as shallow-water archetypes representative of those design classes (Section 3.6). The Oyster, a bottom-hinged nearshore surge flap rated 291 kW, stands in for the WaveRoller class [20]; its matrix, binned in T_{e}, is also given by Silva et al. [16] and is reproduced in Table A4. The Wavestar C6, twenty floats of 6 m diameter on a bottom-standing structure, rated 600 kW with a storm-protection mode that lifts the floats clear of the water above H_{m0} = 4 m, stands in for the Eco Wave Power class; its matrix, binned in the mean zero-crossing period T_{z} and reproduced in Table A5, comes from the specific power matrices performance data of the Roshage prototype programme [21]. Where a matrix is binned in T_{z}, the reanalysis energy period is converted with the JONSWAP-spectrum relation $T_{\mathrm{e}} \approx 1.18\, T_{\mathrm{z}}$.

2.8. Energy Yield, Capacity Factor, and Operating Time

For every three-hourly sea state, the device output was read from the power matrix by bilinear interpolation in H_{m0} and period. Sea states outside the tabulated support, whether below cut-in or beyond the survival limit, return zero. The annual energy production follows from summing over the record and rescaling to one year,

$$\mathrm{AEP} = (8766/N) \sum p(H_{\mathrm{m0},*t*}, T_{*t*}), \tag{5}$$

where N is the number of valid steps and 8766 the mean hours in a year. The capacity factor, the standard figure of merit for comparing generation assets and sites [8,16], is the mean electrical power divided by the rated power,

$$\mathrm{CF} = \langle P_{\mathrm{elec}} \rangle / P_{\mathrm{rated}}. \tag{6}$$

For context, modern offshore wind farms reach capacity factors of about 35–50%, specific power matrix full-scale WEC estimates run from roughly 10–20% at energetic Atlantic sites [22] down to 4–9% in the Mediterranean [3], and about 30% is often quoted as the level at which a wave project becomes economically interesting [3]. Because the rated power is reached only in the strongest tabulated sea states, the relation between installed capacity and the local sea is made explicit by two further quantities computed from the same joint histogram, as follows: the operating fraction, the share of the year in which the matrix returns non-zero output, and the rated fraction, the share of the year at 95% of rated power or more. Section 3.4 reports both alongside the capacity factors they account for.

2.9. Froude Downscaling

Because the three machines were built for rougher water, a scaled family of each was also tested. Under Froude similitude, a geometric scale factor λ (with $\lambda \leq 1$ for a smaller device) transforms the whole power matrix, not only its output, as follows: the wave-height axis, the period axis, and the rated power scale together as

$$H' = \lambda H, \qquad T' = \sqrt{\lambda}\, T, \qquad P' = \lambda^{3.5} P, \tag{7}$$

which is the standard practice for matching ocean devices to milder seas [3,23]. The period transformation is the essential part, as follows: it shifts the resonant response of the device to shorter waves, so a $\lambda = 0.25$ Pelamis responds over roughly 2.5–6.5 s of energy period instead of 5–13 s, which is exactly where the Turkish seas live. The height axis contracts in proportion, so the scaled matrix saturates in the moderate seas that actually occur. For each device and site, the scale was searched over $\lambda = 0.20$ to 1.00 in steps of 0.05, and the value that maximised the annual capacity factor (Equation (6)) was retained. The same search was repeated at every sea cell of the domain to draw the coast-wide maps of Section 3.5. The procedure trades absolute output for a better match to the local spectrum, and Section 3.5 shows how steep that trade is.

3. Results

3.1. Where the Energy Is

Averaged over the twenty years, the wave power flux runs from below 0.1 kW m^{-1} in sheltered corners to 6.5 kW m^{-1} in the open Levantine Sea, with a domain median of 2.8 kW m^{-1} (Figure 3). The richest water sits south of Crete and through the central Aegean, where long northerly fetches under the Etesian regime keep the sea working. The Black Sea holds a smoother maximum of about 3 to 4 kW m^{-1} across its central and western interior and falls away toward the sheltered south-east. The Sea of Marmara is an order of magnitude below its neighbours, with a regional mean of 0.45 kW m^{-1} and a maximum of 0.9 kW m^{-1} in its western half (Table 1). One point matters for what follows: the strongest Levantine cells lie in water far deeper than the devices can use, so the best deployable water is not the most energetic water. It is found off the Bosphorus approaches, on the western Black Sea shelf, and in the southern Aegean instead.

Table 3. The twelve candidate sites (twenty-year means). P is the wave power flux, SV the seasonal variability index (Equation (4)), and COV the coefficient of variation of the three-hourly flux.

Site	Region	Location	Depth (m)	H_{m0} (m)	T_e (s)	P (kW m^{-1})	SV	COV
B1	Black Sea	41.6° N, 28.6° E	80	0.86	4.55	3.41	1.46	2.29
B2	Black Sea	43.8° N, 30.0° E	91	0.91	4.41	3.35	1.51	1.99
B3	Black Sea	44.4° N, 30.6° E	94	0.90	4.31	3.14	1.51	1.90
M1	Marmara	40.6° N, 28.2° E	90	0.46	2.92	0.81	1.14	2.18

https://doi.org/10.3390/en19163923

Table 3. *Cont.*

Site	Region	Location	Depth (m)	H_{m0} (m)	T_e (s)	P (kW m^{-1})	SV	COV
M2	Marmara	40.6° N, 27.4° E	90	0.36	2.93	0.55	1.03	2.22
M3	Marmara	40.4° N, 28.8° E	58	0.21	2.72	0.17	1.21	2.58
A1	Aegean	37.2° N, 25.0° E	94	0.98	4.42	3.55	1.08	1.55
A2	Aegean	37.0° N, 25.6° E	68	0.90	4.26	2.80	1.15	1.49
A3	Aegean	36.8° N, 27.0° E	95	0.91	4.38	2.74	1.16	1.40
L1	Mediterranean	35.2° N, 26.2° E	86	0.94	4.58	3.09	1.08	1.48
L2	Mediterranean	34.4° N, 35.8° E	100	0.55	5.36	1.59	2.06	2.58
L3	Mediterranean	36.4° N, 35.4° E	78	0.53	4.45	1.24	1.87	2.82

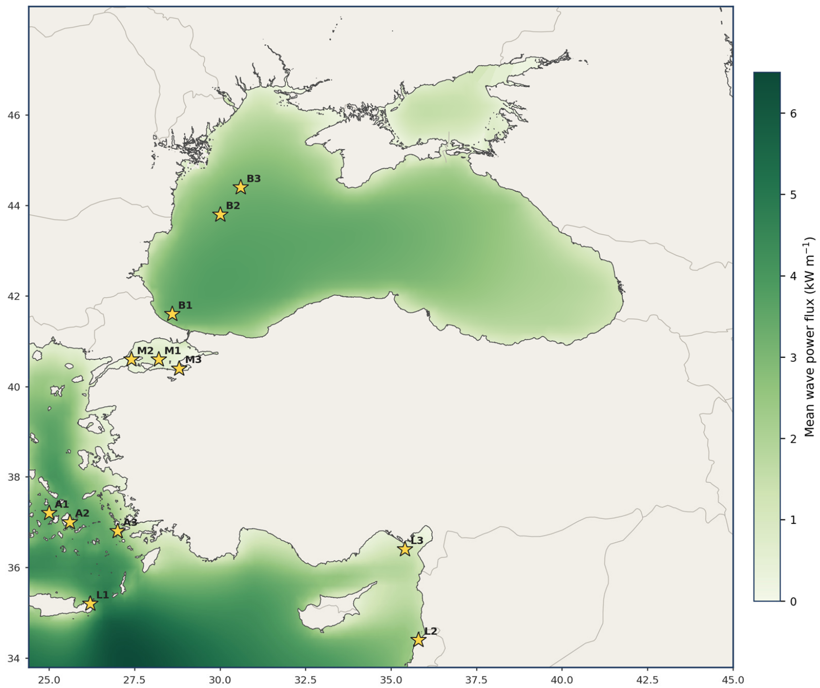

Figure 3. Mean wave power flux (kW m^{-1}) over 2006–2026. Stars mark the twelve candidate sites (codes as in Table 3). The field is drawn from all valid 0.2° cells and clipped at the GEBCO coastline.

3.2. Seasonal and Year-to-Year Variability

The resource is strongly seasonal (Figure 4). Winter flux runs to roughly 1.6 to 2 times the annual mean across both the Black Sea and the Aegean as depressions track through, while spring and autumn are quieter. The central Aegean is the exception, as follows: it carries a second, smaller peak in summer that the steady Etesian winds sustain. That summer energy is useful out of proportion to its size, because it arrives when the basin-wide winter peak has gone and when cooling demand is highest. The mean sea states behind the flux are shown in Figure 5, as follows: across the whole domain the mean energy period stays below about 5.5 s and is usually 4 to 5 s, well short of the 7 to 13 s band the full-scale devices were built for, and in the Marmara it is below 3 s. Mean wave heights stay under 1.2 m almost everywhere. These are short-period seas of moderate height, dominated by locally generated wind waves rather than by remote swell. Year-to-year changes are milder than the seasonal swing (Figure 6). The standard deviation of the annual mean is 10 to 15% of the long-term mean at the seven candidate sites whose flux exceeds 2.5 kW m^{-1} and 20 to 23% at the other five, and the most extreme single years depart from the long-term mean by −30 to +34% and by −36 to +56% respectively. Least-squares trends fitted to the annual means are not significant at any site outside the Marmara ($p > 0.2$ throughout); the three Marmara sites fall by 1.7 to 2.0% a year ($p = 0.02$–0.03) from an already low base.

https://doi.org/10.3390/en19163923

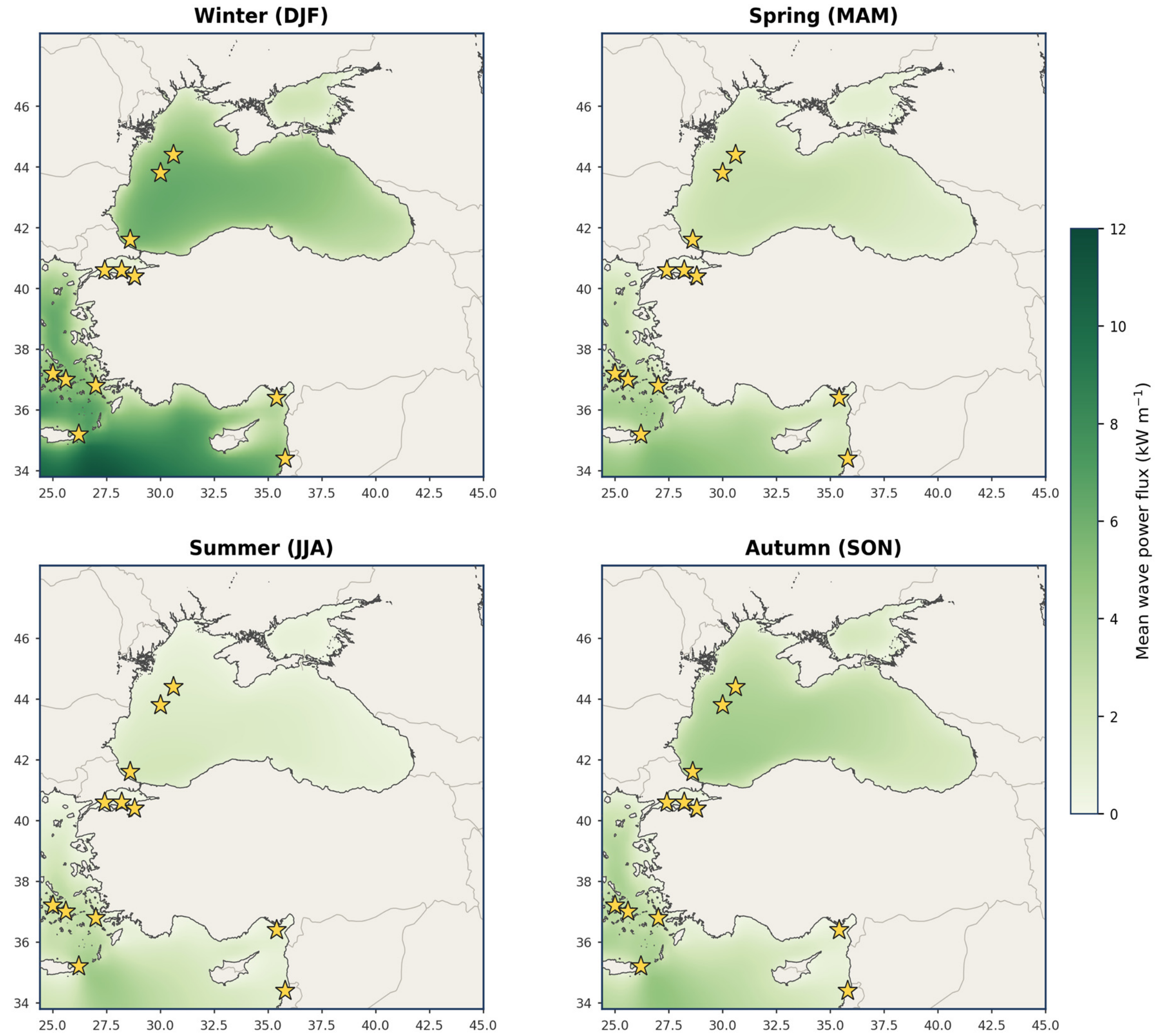

Figure 4. Seasonal mean wave power flux (kW m^{-1}) for winter (DJF), spring (MAM), summer (JJA), and autumn (SON), 2006–2026.

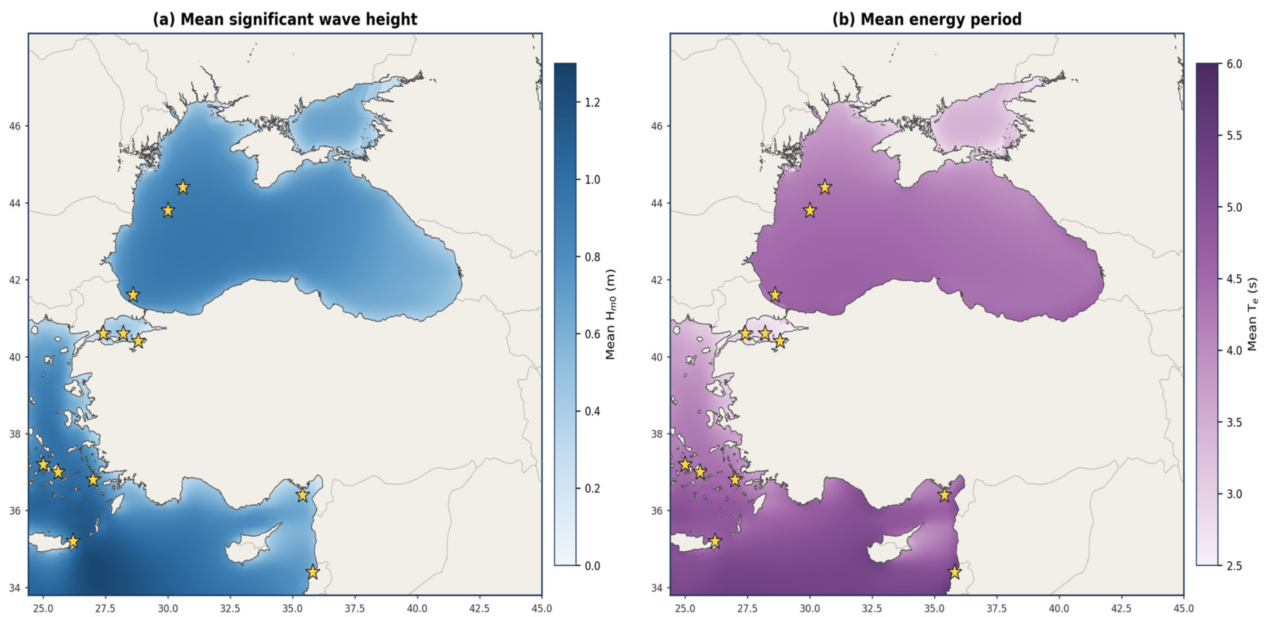

Figure 5. Twenty-year mean fields. (**a**) Significant wave height H_{m0} (m). (**b**) Energy period T_e (s).

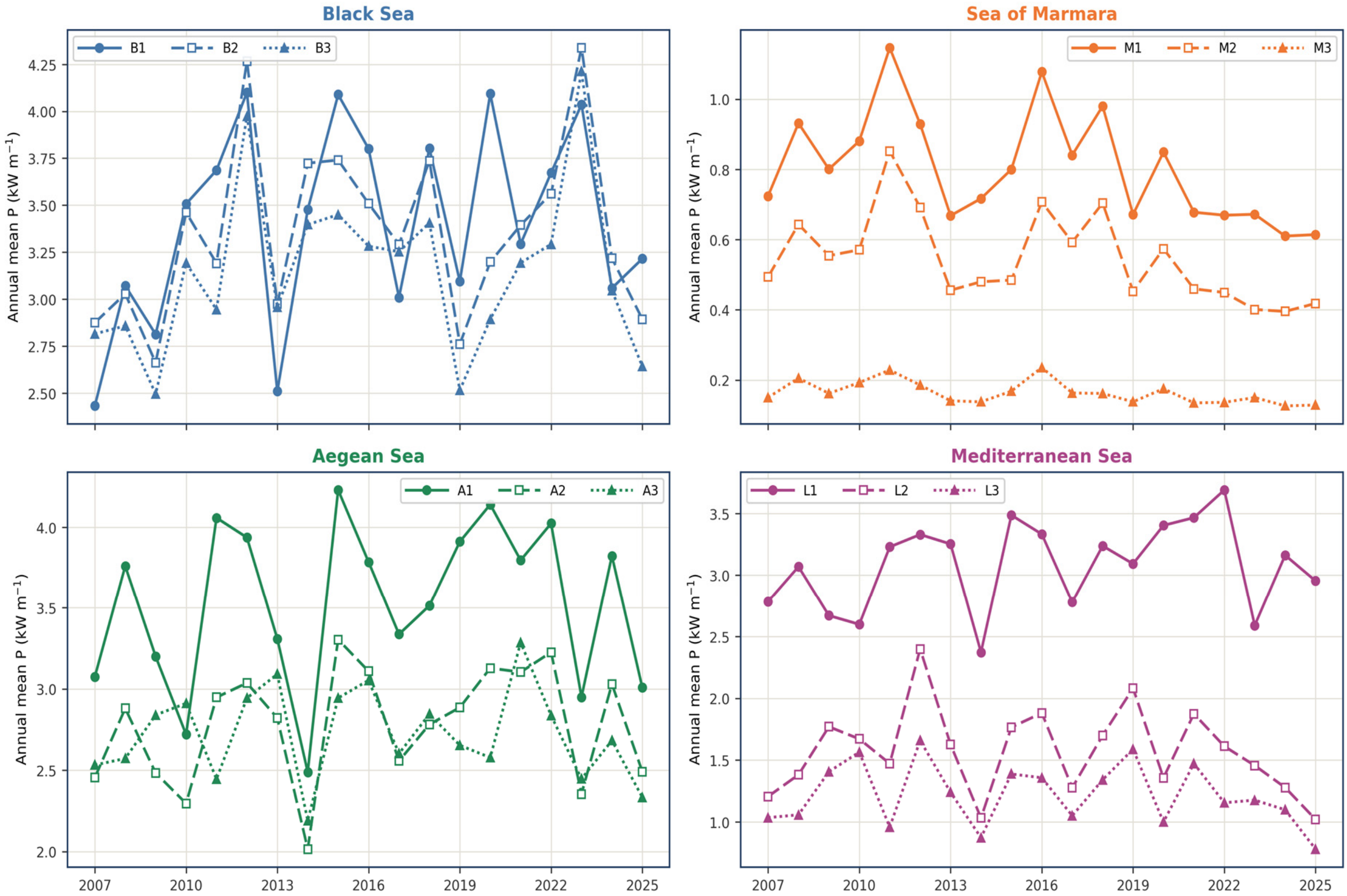

Figure 6. Interannual variability of the annual-mean wave power flux at the twelve candidate sites, for the complete calendar years 2007–2025, grouped by region. Within each region the first site (B1, M1, A1, L1) is drawn with a solid line and filled circles, the second with a dashed line and open squares, and the third with a dotted line and filled triangles.

3.3. The Candidate Sites

The twelve sites, three per region, are listed in Table 3. The Black Sea trio pairs the well-known south-western hotspot off the Bosphorus approaches (B1) with two sites on the western shelf (B2, B3), all at 3.1–3.4 kW m^{-1}. The Aegean trio (A1–A3) spans the Cyclades and the Dodecanese at 2.7–3.6 kW m^{-1}, and the Mediterranean trio runs from east of Crete (L1, 3.1 kW m^{-1}) to the Levantine coast (L2) and İskenderun Bay (L3), where the deployable shelf carries less energy. The Marmara sites (M1–M3) sit at 0.2–0.8 kW m^{-1}, an order of magnitude below the others, and are retained deliberately, as follows: they provide what appears to be the first long-term, device-oriented benchmark for that basin. The joint distribution at B1 and A1 (Figure 7) shows what the spectral matching has to accommodate. The sea sits most often at H_{m0} near 0.5 to 1.5 m and T_e near 3.5 to 5 s, yet most of the energy is delivered by rarer, livelier states at H_{m0} of 1.5 to 3 m and T_e of 5 to 7 s. The everyday sea and the energetic sea are not the same sea, and that split is what a converter has to cope with. The spikiness is real, as follows: the COV of the three-hourly flux is 1.4–2.8 across the sites, and the storm-driven Black Sea and Levantine sites carry the largest seasonal swings (SV up to 2.1). Monthly mean wave power flux at the twelve candidate sites are given in Figure 8.

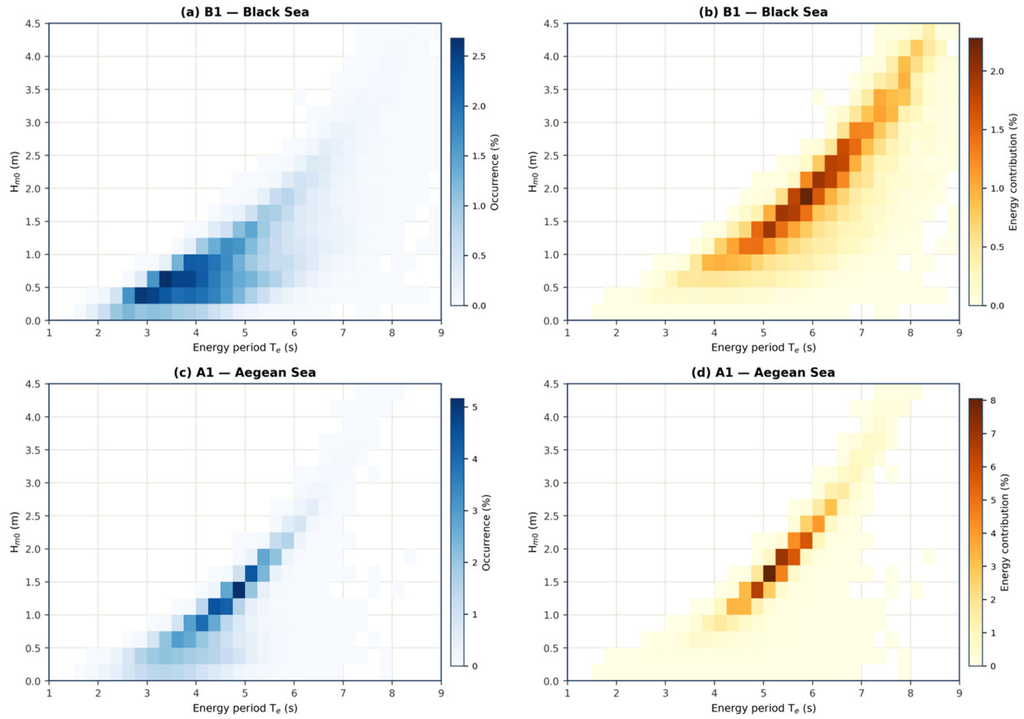

Figure 7. Joint distribution of sea states at sites B1 (Black Sea) and A1 (Aegean): how often each (T_e, H_{m0}) bin occurs (**left**) and how much of the total energy it carries (**right**).

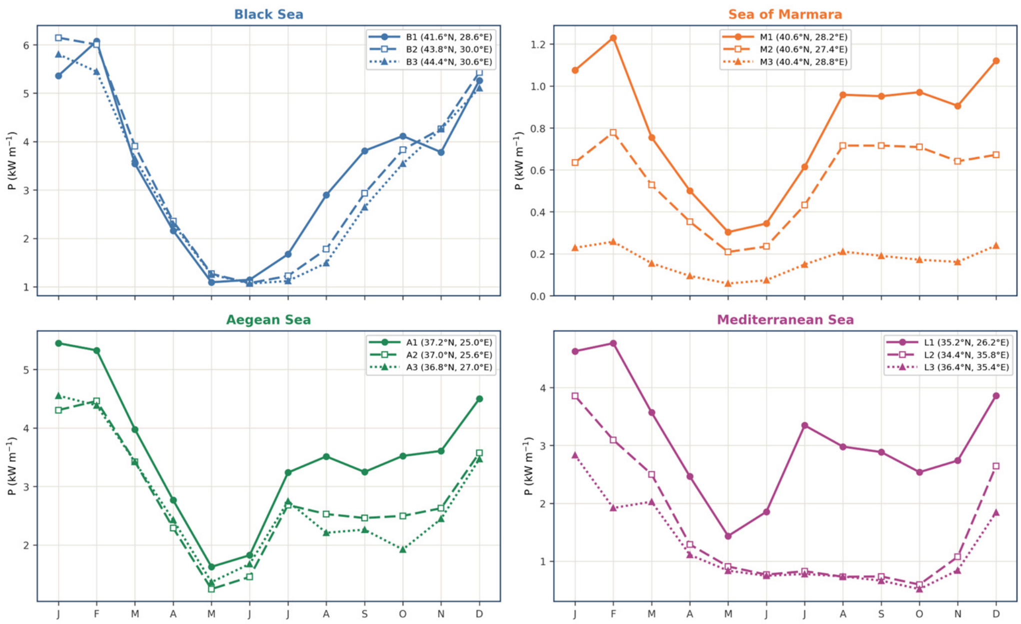

Figure 8. Monthly mean wave power flux at the twelve candidate sites, grouped by region. Note the different vertical scales. Within each region the first site (B1, M1, A1, L1) is drawn with a solid line and filled circles, the second with a dashed line and open squares, and the third with a dotted line and filled triangles.

3.4. Devices at Full Scale

At their original scale, the response bands of the three reference converters overlap a limited part of the regional sea-state distributions (Table 4). Outside the Marmara, the capacity factors span 1.0–3.4% for Pelamis, 0.8–2.8% for AquaBuOY and 0.8–3.1% for Wave Dragon; inside the Marmara, all three are up to 0.4%. The operating statistics of Section 2.8 locate the cause, as follows: at B1 a full-scale Pelamis returns non-zero output for 31% of the year and reaches rated power for 0.0% of it, and the other two devices behave alike. The tabulated rated sea states of all three machines (Appendix A) occur here for a few hours a year at most, so the installed capacity of each is set by a sea state the region does not supply. The ranking across sites follows the resource, with the Black Sea trio and A1 leading. In absolute terms a full-scale Pelamis would make 70–230 MWh a year at the nine sites outside the Marmara and a Wave Dragon 490–1900 MWh, from installed capacities of 750 kW and 7 MW, respectively.

Table 4. Full-scale performance: capacity factor (CF, %) and annual energy production (AEP, MWh yr^{-1}) at each site, computed from the specific power matrices of Appendix A.

Site	Pelamis CF	AEP	AquaBuOY CF	AEP	W. Dragon CF	AEP
B1	3.4	226	2.8	61	2.8	1732
B2	3.1	202	2.4	54	2.8	1698
B3	2.7	179	2.2	48	2.6	1584
M1	0.2	12	0.2	4	0.4	222
M2	0.1	6	0.1	2	0.3	161
M3	0.0	1	0.0	0	0.0	18
A1	2.9	189	2.4	52	3.1	1894
A2	1.8	115	1.5	33	2.3	1411
A3	1.7	115	1.5	32	2.2	1356
L1	2.4	157	1.9	42	2.6	1609
L2	1.5	102	1.1	25	1.1	700
L3	1.0	67	0.8	16	0.8	494

3.5. The Effect of Scaling

Froude scaling improves the spectral alignment substantially, and with it the capacity factor (Table 5, Figure 9). The best scale factors land between 0.20 and 0.25, that is machines one-fifth to one-quarter of their original length, with rated powers cut to about 3–6 kW for the scaled Pelamis, 1–2 kW for the scaled AquaBuOY, and about 25 kW for the scaled Wave Dragon. At those sizes, the capacity factor climbs into a useful range at the seven energetic sites, those whose mean flux exceeds 2.5 kW m^{-1} (B1–B3, A1–A3 and L1): 32–46% for Pelamis, 30–40% for AquaBuOY and 37–47% for Wave Dragon, nine to twenty-seven times the full-scale values and above the 30% level usually taken as the threshold of economic interest [3]. The two weaker Levantine sites reach 13–25%, and even the Marmara reaches 8–27% once the devices are scaled, demonstrating that spectral alignment benefits even the least energetic basin. The operating statistics move the same way, as follows: at B1 the $\lambda = 0.25$ Pelamis is producing 80% of the year instead of 31%. Figure 10 extends the result along every coast of the domain, as follows: the whole Black Sea rim, the Aegean archipelago, and the Levantine shore all support scaled capacity factors above 25–30%, with the optimal λ between 0.20 and 0.30 almost everywhere, so the design target is nearly the same in four very different seas. The energy column of Table 5 sets the form the deployment would take. At the seven energetic sites, a scaled Pelamis unit makes 16–23 MWh a year, a scaled AquaBuOY 5–7 MWh, and a scaled Wave Dragon 82–104 MWh, and at the nine sites outside the Marmara the ranges widen to 5–23, 2–7 and 49–104 MWh, so practical deployment would take the form of a modular array of many small machines rather than a handful of large ones, which shifts the engineering problem from the single device toward the array; Section 4 returns to this.

Table 5. Best Froude-scaled performance at each site: optimal geometric scale λ, scaled rated power P_r (kW), capacity factor (CF, %), and annual energy production (AEP, MWh yr^{-1}), for each of the three devices.

Site	Pel. λ	P_r	CF	AEP	AqB λ	P_r	CF	AEP	W.D. λ	P_r	CF	AEP
B1	0.25	5.9	31.9	16.4	0.25	2.0	29.5	5.1	0.20	25.0	37.3	81.8
B2	0.25	5.9	38.8	20.0	0.25	2.0	34.5	5.9	0.20	25.0	42.1	92.5
B3	0.25	5.9	39.7	20.4	0.25	2.0	34.9	6.0	0.20	25.0	41.8	91.8
M1	0.20	2.7	27.4	6.5	0.25	2.0	19.8	3.4	0.20	25.0	22.9	50.3
M2	0.20	2.7	20.6	4.9	0.25	2.0	15.3	2.6	0.20	25.0	18.4	40.4
M3	0.20	2.7	9.7	2.3	0.20	0.9	8.6	0.7	0.20	25.0	7.7	16.8
A1	0.25	5.9	45.1	23.2	0.25	2.0	35.2	6.0	0.20	25.0	40.5	88.9
A2	0.25	5.9	45.5	23.4	0.25	2.0	38.2	6.5	0.20	25.0	43.7	96.0
A3	0.25	5.9	45.6	23.4	0.25	2.0	39.5	6.8	0.20	25.0	46.6	102.4
L1	0.25	5.9	44.8	23.0	0.25	2.0	39.1	6.7	0.20	25.0	47.1	103.5
L2	0.25	5.9	13.4	6.9	0.25	2.0	15.9	2.7	0.20	25.0	22.1	48.5
L3	0.20	2.7	21.1	5.0	0.20	0.9	20.2	1.6	0.20	25.0	25.2	55.3

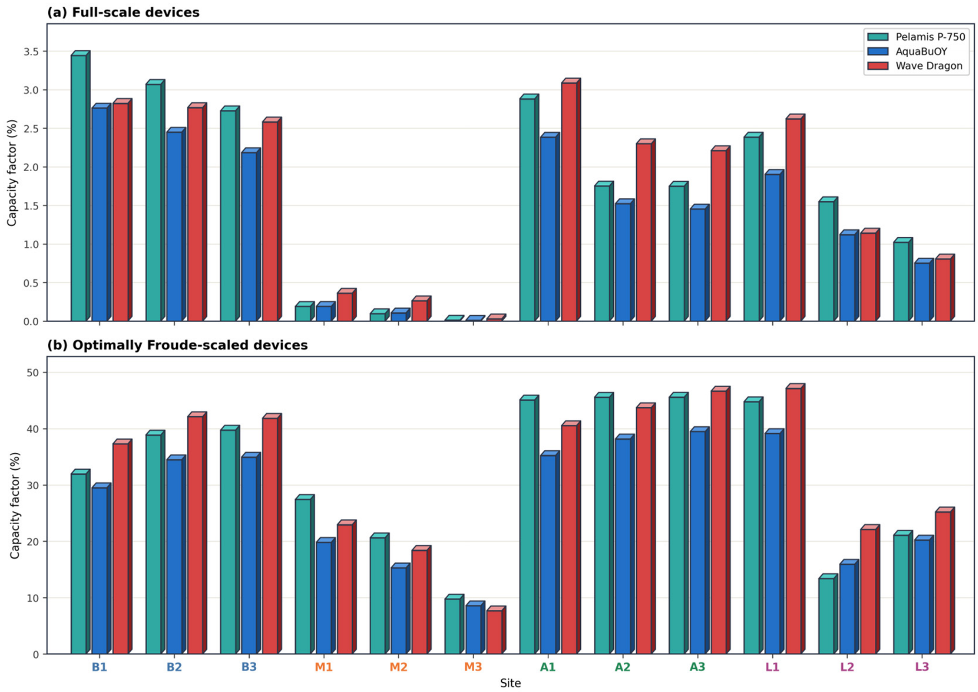

Figure 9. Capacity factor of the three converters at the twelve sites, (**a**) at full scale and (**b**) after the best Froude scaling. Site codes are coloured by region as in Figures 6 and 8.

3.6. Archetypes of the Current Device Classes

The two shallow-water archetypes behave differently from the three ocean devices, and better (Table 6, Figure 11). At full scale, the Oyster surge flap reaches capacity factors of 7–10% at the seven energetic sites and the Wavestar 15–19% (3–10% and 6–19% across all nine sites outside the Marmara), that is three to eight times the full-scale values of Pelamis, AquaBuOY, and Wave Dragon at the same sites, because both machines were designed for short, moderate seas in the first place, as follows: the Oyster responds from 5 s energy period upward, and the Wavestar produces from about 3 s of zero-crossing period at half a metre of wave. Scaling still helps. At their best Froude scale, the archetypes reach 49–59% at the seven energetic sites, 35–48% at the two weaker Levantine sites, and 21–39% in the Marmara, and the Wavestar keeps usefully large scaled ratings—up to 53 kW at A1, where its optimum is λ = 0.50—because its storm-protection cut-off means the full-size machine already fits much of the local wave climate. The coast-wide maps (Figure 12) repeat the pattern of Figure 10 at a higher level, as follows: the whole Black Sea rim, the Aegean, and the Levantine shore support scaled capacity factors above 45–50% for both archetypes. These results transfer to the named commercial devices only as far as the archetypes represent them, but the direction is consistent, as follows: shallow-water archetypes representative of contemporary design classes start considerably closer to the regional specification than the ocean-scale devices of Section 3.4.

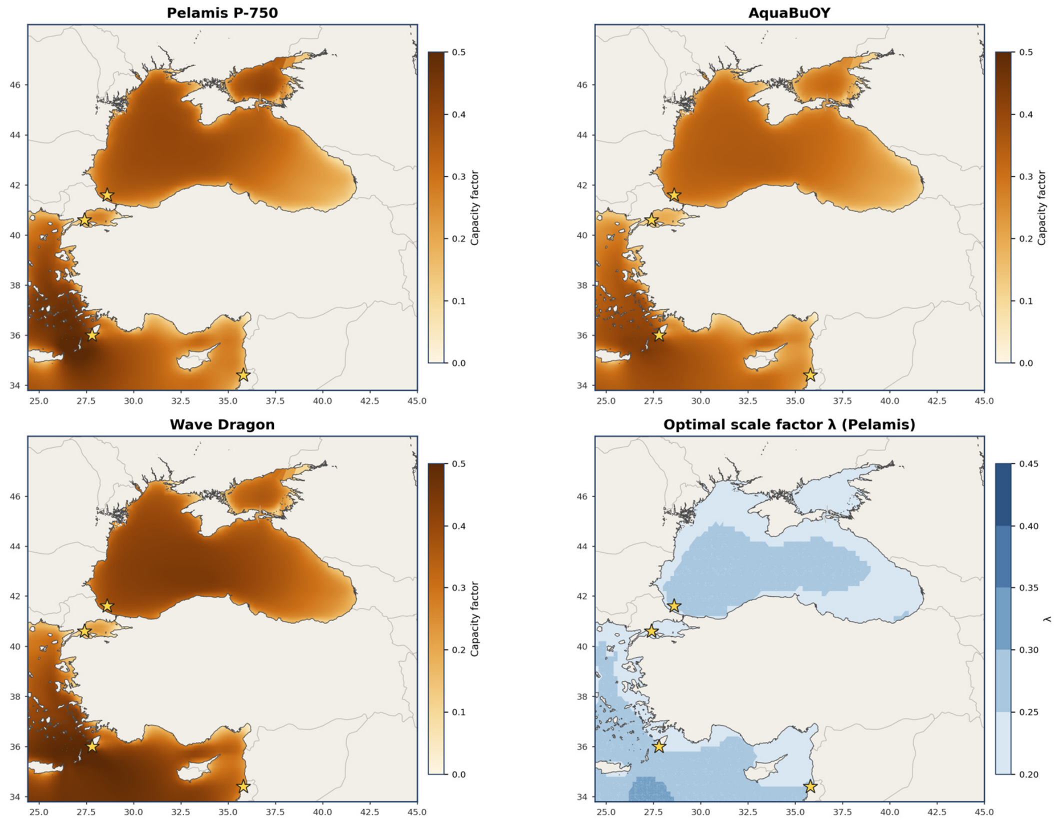

Figure 10. Coast-wide view of the scaling result: capacity factor of the optimally Froude-scaled Pelamis, AquaBuOY and Wave Dragon over the whole domain, and the optimal scale factor λ for Pelamis. Stars mark the best deployable site of each region.

Table 6. Performance of the two shallow-water archetypes at the twelve sites: full-scale capacity factor (CF, %), optimal scale λ, scaled rated power P_r (kW), scaled capacity factor, and scaled annual energy production (AEP, MWh yr^{-1}).

Site	Oy. CF_{full}	λ	P_r	CF	AEP	Wst. CF_{full}	λ	P_r	CF	AEP
B1	9.3	0.25	2.3	50.8	10.1	15.9	0.30	8.9	49.5	38.5
B2	9.1	0.25	2.3	54.8	10.9	16.5	0.30	8.9	51.4	40.0
B3	8.4	0.25	2.3	54.4	10.8	15.7	0.30	8.9	50.6	39.3
M1	0.8	0.20	1.0	38.9	3.6	3.3	0.25	4.7	34.3	14.1
M2	0.5	0.20	1.0	32.3	3.0	2.3	0.25	4.7	29.9	12.3
M3	0.1	0.20	1.0	21.0	1.9	0.4	0.20	2.1	28.0	5.3
A1	10.0	0.30	4.3	52.5	19.8	18.7	0.50	53.0	48.7	226.4
A2	6.6	0.30	4.3	55.5	20.9	14.8	0.40	24.3	51.3	109.2
A3	6.7	0.25	2.3	59.1	11.8	14.8	0.40	24.3	54.6	116.2
L1	8.4	0.25	2.3	58.9	11.7	16.9	0.40	24.3	55.3	117.7
L2	4.3	0.25	2.3	35.4	7.1	8.9	0.25	4.7	44.6	18.3
L3	2.9	0.20	1.0	44.2	4.0	6.3	0.25	4.7	47.8	19.7

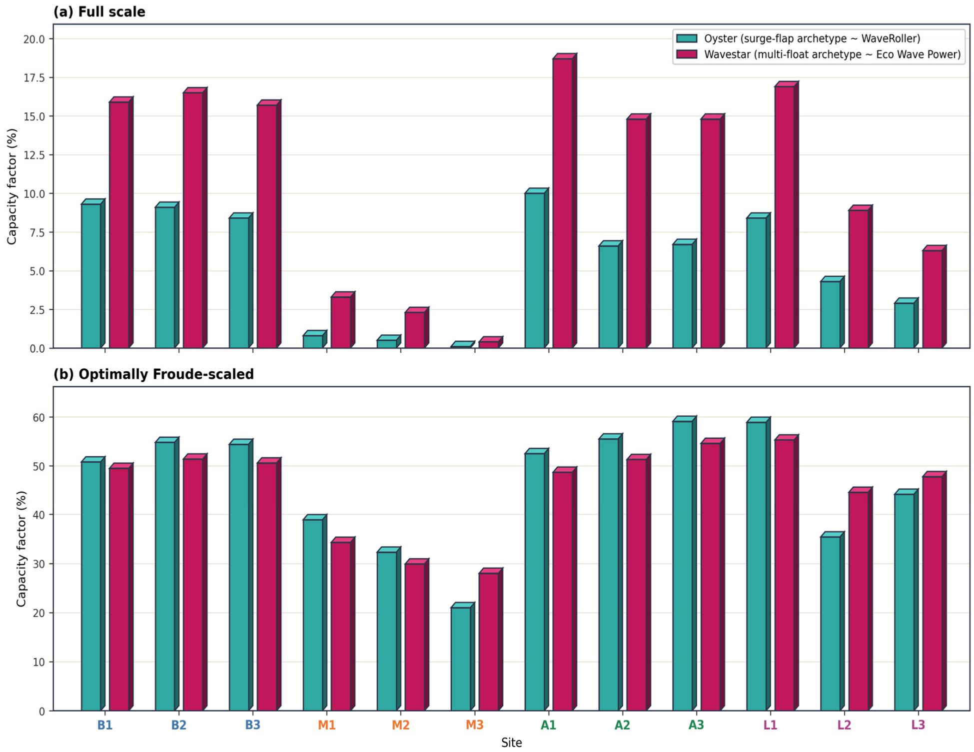

Figure 11. Capacity factor of the two shallow-water archetypes at the twelve sites, (**a**) at full scale and (**b**) after the best Froude scaling. The Oyster surge flap stands in for the WaveRoller class and the Wavestar multi-float machine for the Eco Wave Power class.

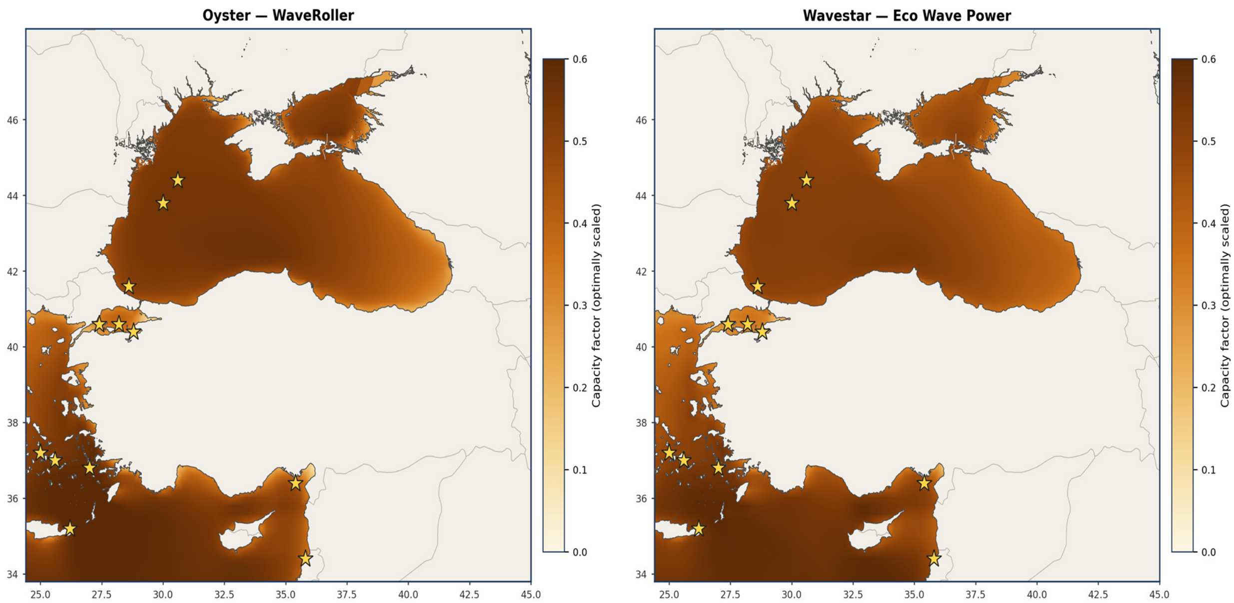

Figure 12. Coast-wide capacity factor of the optimally Froude-scaled archetypes. Stars mark the twelve candidate sites.

It should be noted that all capacity-factor and annual-energy-production results presented above are theoretical predictions based on published power matrices and Froude-similarity scaling. Several practical engineering effects, including maintenance downtime, biofouling, mooring-system losses, and hydrodynamic interference between array devices, are not incorporated in the calculation. Therefore, the numerical values represent upper-bound theoretical performance and are intended primarily for comparative screening among candidate sites and device concepts, rather than representing real-world operational outputs.

4. Discussion

The picture that emerges is consistent and physically sensible. The seas around Türkiye hold a wave resource consistent with semi-enclosed basins, 3.1 to 3.6 kW m^{-1} at the best deployable sites, roughly a tenth of the 20 to 40 kW m^{-1} on the Atlantic margin [1], yet in line with other estimates for the Mediterranean and the Black Sea [3,5,7]. The feature that governs conversion is not the size of the resource but its position in the spectrum. Energy periods of 4 to 5 s sit outside the design band of the mainstream converters, so the response band of a full-scale machine sits largely outside the observed sea-state distribution. The Marmara is the end member of that pattern, as follows: a sheltered basin whose 2.7–2.9 s seas sit almost entirely outside the response bands of the full-scale devices.

The full-scale capacity factors found here, up to 3.4%, sit at or below the power matrix Mediterranean range, which is what the shorter Aegean and Black Sea periods would predict. Sierra et al. [10] reported roughly 10%, 9%, and 11% for Pelamis; AquaBuOY and Wave Dragon at Menorca; Aoun et al. [11] about 5%, 5%, and 4% off Lebanon; and Bozzi et al. [3] 4 to 9% across the basin. The scaling result is quantitatively consistent as well, as follows: cutting each device to one-fifth to one-quarter of its size lifts the capacity factor to 30–47% at the energetic sites, against best sizes of one-quarter to one-third and factors above 30% in the Mediterranean analysis of Bozzi et al. [3]. Two independent analyses landing in the same place, now across four basins rather than one, is a reasonable basis for a design rule, as follows: in seas like these, the route to a usable wave converter runs through small, purpose-built machines in arrays rather than through full-scale ocean devices moved south. The summer Aegean peak adds to the case, since it lines up with the cooling-demand season and runs counter to the winter-heavy wind resource and broadly with the summer-heavy solar one, which could ease the integration of all three.

Array deployment moves the engineering priorities toward mooring layout, electrical aggregation, and maintenance access, and the unit ratings set the scale of each. Replacing one 750 kW machine with $\lambda = 0.25$ units of 6 kW rated power means roughly 125 devices for the same installed capacity, and about 40 devices per installed megawatt even at the scaled Wave Dragon rating of 25 kW. With inter-device spacing of a few device lengths, a 1 MW scaled-Pelamis farm would occupy on the order of one square kilometre of sea surface and several hundred mooring lines and electrical jumpers. The logistical load therefore shifts from the single hull to mooring layout, electrical aggregation at low voltage, and above all maintenance access, which favours sites close to harbours, as follows: B1 lies under 30 km off the Thracian coast and about 60 km from the northern entrance of the İstanbul strait, and the Aegean and İskenderun sites are all within reach of regional ports. Spatial competition must also be respected. The B1 area lies near one of the densest shipping approaches in the world, the Marmara is effectively a shipping lane end to end, and the Aegean sites sit in waters shared with ferry routes, fisheries and, seasonally, intense tourism; array permitting in these zones will constrain layouts at least as strongly as the hydrodynamics. None of these constraints is prohibitive for the hectare-scale pilot arrays that the resource justifies, but they belong in any techno-economic follow-up.

The device set is deliberately classical. Pelamis and AquaBuOY are treated as legacy reference technologies, and all three devices are included as specific power matrix benchmark rather than as procurement-ready products. Their power matrices and their behaviour is well documented [9,16], which keeps every number in this paper reproducible and comparable with two decades of literature. Technology has moved on since, and Table 7 profiles four devices in current development [24]. The CorPower C4 is a phase-controlled point absorber whose pretension system broadens the response band; it survives storms by detuning and letting the waves pass over the buoy, and a grid-connected unit ran through the winter of 2023–2024 off Aguçadoura, Portugal [25]. The CETO absorber is fully submerged and rides out extreme seas below the surface turbulence [26]. The Eco Wave Power system mounts floaters on breakwaters and piers and lifts them clear of the water when the sea turns rough; a 100-kW pilot has been grid-connected in the Port of Jaffa. The WaveRoller is a bottom-hinged surge flap that works on the seabed in 8–20 m of water, its bottom-heavy body sitting below the worst of the surface motion [20].

Table 7. Four current wave energy converters discussed in the text: placement, rated power, sea-keeping strategy, and demonstration status. None publishes a power matrix, so they are compared qualitatively.

Device (Developer, Country)	Placement	Rated Power	Sea-Keeping Strategy	Status
CorPower C4 (CorPower Ocean, Sweden)	Offshore, surface point absorber	300 kW	Detunes and lets storm waves pass over the buoy	Grid-connected demonstration, Aguçadoura, Portugal, 2023–2024
CETO (Carnegie Clean Energy, Australia)	Offshore, fully submerged point absorber	240 kW (CETO 5); MW-class design (CETO 6)	Operates below the surface turbulence	Grid-connected array off Perth, 2015; next generation in development
Eco Wave Power (Israel/Sweden)	Coastal; floaters on breakwaters and piers	100 kW pilot (EWP-EDF One)	Floaters are lifted out of the water in storms	Grid-connected pilots, Gibraltar and Port of Jaffa
WaveRoller (AW-Energy, Finland)	Nearshore seabed, 8–20 m; bottom-hinged surge flap	350 kW to 1 MW class	Bottom-heavy body fully submerged below surface motion	Grid-connected at Peniche, Portugal, since 2019

None of the four publishes a power matrix, so none can be computed as itself. Section 3.6 instead quantifies two of the classes through their archetypes, the Oyster surge flap for the WaveRoller and the Wavestar multi-float machine for Eco Wave Power, and finds full-scale capacity factors three to eight times those of the ocean devices, with scaled values of 49–59% at the energetic sites. The remaining two classes can be bracketed. The heaving point absorber is already represented in the main analysis by AquaBuOY, and tank tests of the C4 report that its phase control roughly triples the absorbed power of an equivalent passive buoy [25], which would lift the scaled point-absorber results of Table 5 accordingly rather than change their geography. The submerged CETO shares the resonance physics of the surface absorbers; what submergence buys is survivability rather than a different resource. These remain archetype results, and they represent the named commercial devices only as far as the archetypes do.

The regional implications follow from that comparison. The C4 is the closest commercial embodiment of the small resonant machine this analysis keeps arriving at, and its response can be tuned toward the 4–5 s energy periods found here. The submerged CETO suits the storm-exposed Black Sea and Levantine sites, where the ninety-ninth-percentile flux runs to seven to twelve times the mean. The breakwater-mounted Eco Wave Power concept fits the harbours of the Marmara and the Aegean, where it can use existing structures and where our results place a free-floating full-scale machine well outside its response band. The WaveRoller works inside the surf zone, shoreward of anything a 0.2° grid resolves, so the Oyster-based numbers of Section 3.6 should be read as an offshore-boundary estimate, with the coastal modelling flagged below as a precondition for sitting it. Repeating this analysis with manufacturer matrices for any of the four, ideally at the twelve sites of Table 3, remains the natural next step.

Several regional characteristics strengthen the development case beyond the mean flux alone. The first is proximity. The deployable 25–100 m band follows the coast closely along most of the Black Sea rim and through the Aegean archipelago, so cable runs are short, and the harbours that already serve fishing and ferry traffic are the same harbours that would serve maintenance. The second is that the design storm is mild in absolute terms.

The largest significant wave height anywhere in the twenty-year record at the twelve sites is 6.5 m, and the ninety-ninth-percentile flux is seven to eleven times the mean at the energetic sites; that ratio is severe, but the loads it implies are a fraction of those an Atlantic machine is built to survive, which is where much of the structural cost of a full-scale converter goes. The third is timing. The central Aegean carries a summer Etesian peak that arrives when cooling demand is highest and when the winter-dominated wind resource is at its weakest, while the Black Sea and Levantine maxima fall in winter, when solar output is lowest; wave output is therefore out of phase with one or other of the two renewables in every basin of the domain. The fourth is that the specification is stable across the domain. Because the optimal scale sits between 0.20 and 0.30 along essentially every coast (Figure 10), one small machine, designed once for a 4–5 s sea, would suit four hydrographically different basins, which is a manufacturing and supply-chain argument as much as a hydrodynamic one. Taken together, these place the binding constraint identified in this paper on the device rather than on the resource, and of the two it is the tractable one.

Several limits frame these numbers. The 0.2° reanalysis does not resolve shoaling, refraction, or the sheltering of small islands, so a real project would need a high-resolution coastal wave model to pin down site yields; this matters most in the Marmara, which the grid resolves with only 37 cells, and around the Aegean islands. The analysis assumes deep-water flux and uses generic power matrices, and it reports a technical capacity factor that ignores availability, transmission, and array interaction losses, so the device numbers are best read as comparative rather than absolute. Froude scaling keeps the hydrodynamics similar but says nothing about whether a structure one-quarter the size is cheaper per kilowatt, easier to mass-produce, or survivable in the November storms that both the Black Sea and Levantine records contain; small devices can, however, be submerged or de-rated in extremes more readily than large ones. The study also stops short of levelised cost, grid connection, environmental effect, and detailed marine spatial planning. Each of these is a natural next step rather than a flaw in the present result, and for several of them, precedents demonstrating the methodological template (e.g., physics-informed feature engineering and SHAP-based interpretability for wave forecasting [27,28]; spatially-aware machine learning for high-resolution bathymetric mapping [29]; mixed finite element formulations for laminated composite shells [30]; and hybrid wavelet-fuzzy time series approaches for hydrological prediction [31]) already exist in the literature, all of which are directly transferable to the site-level assessments, device-response analyses, structural survivability evaluations, and environmental forecasting proposed here.

5. Conclusions

Twenty years of Copernicus Marine reanalysis, GEBCO bathymetry, and the specific power matrices of three reference converters were combined to assess wave energy conversion across the four seas around Türkiye, with the Black Sea, the Sea of Marmara, the Aegean, and the Eastern Mediterranean treated as four regions of one consistently processed domain and three candidate sites selected per region inside the 25–100 m screening band. The mean flux reaches 6.5 kW m^{-1} in the open Levantine and 3.1–3.6 kW m^{-1} at the best deployable sites, which lie off the Bosphorus approaches, on the western Black Sea shelf, and in the southern Aegean; the Marmara holds an order of magnitude less. Because the seas are short-period, with energy periods near 4 to 5 s, the full-scale Pelamis, AquaBuOY, and Wave Dragon reach capacity factors of up to 3.4%. Froude scaling to one-fifth to one-quarter of the original linear dimensions raises that to 30–47% at the seven energetic sites, at rated powers of roughly 2–25 kW, and the coast-wide maps show both the achievable capacity factor and the optimal scale to be nearly uniform along the Black Sea rim, the Aegean archipelago, and the Levantine shore. The two shallow-water archetypes, representative of contemporary design classes, reach 7–19% at full scale and 49–59% once scaled, so those classes begin closer to the regional specification. That specification is compact and changes little between basins, as follows: a converter tuned to an energy period of 4 to 5 s and a mean wave height near one metre, rated from a few kilowatts to a few tens of kilowatts, moored in 25 to 100 m of water within a short cable run of the coast, and deployed in modular arrays. Refining calls for a high-resolution coastal wave model, manufacturer matrices for the modern small-rated device families as they become available, and a marine spatial-planning assessment of the candidate areas. Rather than issuing a binary verdict on regional feasibility, the analysis defines a consistent converter specification for Türkiye's short-period seas and establishes the technical basis for higher-resolution modelling, prototype selection, and techno-economic assessment.

It should be emphasised that the conclusion favouring small-scale modular wave-energy-converter arrays along the Black-Sea, Aegean, and Levantine coasts is a theoretical inference derived from 20-year re-analysis datasets. This outcome serves for regional potential evaluation and device-concept screening only and shall not be directly used as decision-making evidence for real-world project investment and construction. Further validation including tank tests, open-sea prototype trials, and high-resolution site-specific modelling is still required.

Funding: This research received no external funding.

Data Availability Statement: The wave reanalysis is available from the Copernicus Marine Service (product cmems_mod_glo_wav_my) at https://marine.copernicus.eu. Bathymetry is from the GEBCO 2026 Grid at https://www.gebco.net. Derived data and analysis code are available from the author on request. All device-specific power matrices utilized for the annual energy production calculations are reproduced in the Appendix A of this paper. No new in situ observational data were generated in this study; all calculations are built upon open-access public datasets.

Conflicts of Interest: The author declares no conflicts of interest.

Appendix A Power Matrices of the Reference Converters

Tables A1–A5 reproduce the power matrices used in this study. Entries are electrical output in kW; empty cells and zeros denote sea states outside the operating envelope. The Pelamis and Oyster matrices are binned in energy period T_e and the AquaBuOY and Wave Dragon matrices in peak period T_p, all as published by Silva et al. [16]; the Wavestar matrix is binned in zero-crossing period T_z, as published in the Roshage prototype performance data [26] (Section 2.7).

Table A1. Pelamis P-750 power matrix (kW), binned by T_e (s, columns) and H_{m0} (m, rows) [16].

H_{m0} (m)	5	5.5	6	6.5	7	7.5	8	8.5	9	9.5	10	10.5	11	11.5	12	12.5	13
0.5	0	0	0	0	0	0	0	0	0	0	0	0	0	0	0	0	0
1	0	22	29	34	37	38	38	37	35	32	29	26	23	21	0	0	0
1.5	32	50	65	76	83	86	86	83	78	72	65	59	53	47	42	37	33
2	57	88	115	136	148	153	152	147	138	127	116	104	93	83	74	66	59
2.5	89	138	180	212	231	238	238	230	216	199	181	163	146	130	116	103	92
3	129	198	260	305	332	340	332	315	292	266	240	219	210	188	167	149	132
3.5	0	270	354	415	438	440	424	404	377	362	326	292	260	230	215	202	180
4	0	0	462	502	540	546	530	499	475	429	384	366	339	301	267	237	213
4.5	0	0	544	635	642	648	628	590	562	528	473	432	382	356	338	300	266
5	0	0	0	739	726	731	707	687	670	607	557	521	472	417	369	348	328
5.5	0	0	0	750	750	750	750	750	737	667	658	586	530	496	446	395	355
6	0	0	0	0	750	750	750	750	750	750	711	633	619	558	512	470	415
6.5	0	0	0	0	750	750	750	750	750	750	750	743	658	621	579	512	481
7	0	0	0	0	0	750	750	750	750	750	750	750	750	676	613	584	525
7.5	0	0	0	0	0	0	750	750	750	750	750	750	750	750	686	622	593
8	0	0	0	0	0	0	0	750	750	750	750	750	750	750	750	690	625

Table A2. AquaBuOY power matrix (kW), binned by T_p (s, columns) and H_{m0} (m, rows) [16].

H_{m0} (m)	5	6	7	8	9	10	11	12	13	14	15	16	17
1	0	0	8	11	12	11	10	8	7	0	0	0	0
1.5	0	13	17	25	27	26	23	19	15	12	12	12	7
2	0	24	30	44	49	47	41	34	28	23	23	23	12
2.5	0	37	47	69	77	73	64	54	43	36	36	36	19
3	0	54	68	99	111	106	92	77	63	51	51	51	27
3.5	0	0	93	135	152	144	126	105	86	70	70	70	38
4	0	0	0	122	176	198	188	164	137	112	91	91	49
4.5	0	0	0	223	250	239	208	173	142	115	115	115	62
5	0	0	0	250	250	250	250	214	175	142	142	142	77
5.5	0	0	0	250	250	250	250	250	211	172	172	172	92

Table A3. Wave Dragon power matrix (kW), binned by T_p (s, columns) and H_{m0} (m, rows) [16].

H_{m0} (m)	5	6	7	8	9	10	11	12	13	14	15	16	17
1	160	250	360	360	360	360	360	360	320	280	250	220	180
2	640	700	840	900	1190	1190	1190	1190	1070	950	830	710	590
3	0	1450	1610	1750	2000	2620	2620	2620	2360	2100	1840	1570	1310
4	0	0	2840	3220	3710	4200	5320	5320	4430	3930	3440	2950	2460
5	0	0	0	4610	5320	6020	7000	7000	6790	6090	5250	3950	3300
6	0	0	0	0	6720	7000	7000	7000	7000	7000	6860	5110	4200
7	0	0	0	0	0	7000	7000	7000	7000	7000	7000	6650	5740

Table A4. Oyster power matrix (kW), binned by T_e (s, columns) and H_{m0} (m, rows) [16].

H_{m0} (m)	5	6	7	8	9	10	11	12	13
0.5	0	0	0	0	0	0	1	3	3
1	20	30	38	42	44	44	45	47	45
1.5	80	85	92	97	102	103	104	100	104
2	140	147	152	158	155	155	160	161	156
2.5	192	197	208	202	203	209	211	201	204
3	241	237	237	241	243	230	236	231	235
3.5	0	271	272	269	268	267	270	260	260
4	0	291	290	290	280	287	276	278	277
4.5	0	291	290	290	280	287	276	278	277
5	0	0	290	290	280	287	276	278	277
5.5	0	0	290	290	280	287	276	278	277
6	0	0	290	290	280	287	276	278	277

Table A5. Wavestar C6 (600 kW) power matrix (kW), binned by T_z (s, columns) and H_{m0} (m, row centres); output is zero above H_{m0} = 4 m because the floats are lifted into storm protection [26].

H_{m0} (m)	1	2	3	4	5	6	7	8	9	10	11	12	13	14	15
0.25	0	0	0	0	0	0	0	0	0	0	0	0	0	0	0
0.75	0	0	0	46	71	85	89	88	84	79	74	69	66	62	59
1.25	0	0	50	121	182	212	215	206	192	178	166	155	145	136	128
1.75	0	0	95	231	339	381	374	350	322	296	274	254	237	222	208
2.25	0	0	154	375	535	579	554	511	466	426	391	361	336	314	295
2.75	0	0	228	552	600	600	600	600	600	563	516	475	441	412	386
3.25	0	40	319	600	600	600	600	600	600	600	600	593	550	513	480
3.75	0	53	425	600	600	600	600	600	600	600	600	600	600	600	577
4.25	0	0	0	0	0	0	0	0	0	0	0	0	0	0	0

References

1. Gunn, K.; Stock-Williams, C. Quantifying the global wave power resource. *Renew. Energy* **2012**, *44*, 296–304. [CrossRef]
2. Mørk, G.; Barstow, S.; Kabuth, A.; Pontes, M.T. Assessing the global wave energy potential. In Proceedings of the ASME 29th International Conference on Ocean, Offshore and Arctic Engineering, Shanghai, China, 6–11 June 2010; pp. 447–454.
3. Bozzi, S.; Besio, G.; Passoni, G. Wave power technologies for the Mediterranean offshore: Scaling and performance analysis. *Coast Eng.* **2018**, *136*, 130–146. [CrossRef]

4. Liberti, L.; Carillo, A.; Sannino, G. Wave energy resource assessment in the Mediterranean, the Italian perspective. *Renew. Energy* **2013**, *50*, 938–949. [CrossRef]
5. Akpınar, A.; Kömürcü, M.İ. Assessment of wave energy resource of the Black Sea based on 15-year numerical hindcast data. *Appl. Energy* **2013**, *101*, 502–512. [CrossRef]
6. Aydoğan, B.; Ayat, B.; Yüksel, Y. Black Sea wave energy atlas from 13 years hindcasted wave data. *Renew. Energy* **2013**, *57*, 436–447. [CrossRef]
7. Sağlam, M.; Sulukan, E.; Uyar, T.S. Wave energy and technical potential of Turkey. *J. Nav. Sci. Eng.* **2010**, *6*, 34–50.
8. Carballo, R.; Iglesias, G. A methodology to determine the power performance of wave energy converters at a particular coastal location. *Energy Convers. Manag.* **2012**, *61*, 8–18. [CrossRef]
9. Babarit, A.; Hals, J.; Muliawan, M.J.; Kurniawan, A.; Moan, T.; Krokstad, J. Numerical benchmarking study of a selection of wave energy converters. *Renew. Energy* **2012**, *41*, 44–63. [CrossRef]
10. Sierra, J.P.; Mösso, C.; González-Marco, D. Wave energy resource assessment in Menorca (Spain). *Renew. Energy* **2014**, *71*, 51–60. [CrossRef]
11. Aoun, N.S.; Harajli, H.A.; Queffeulou, P. Preliminary appraisal of wave power prospects in Lebanon. *Renew. Energy* **2013**, *53*, 165–173. [CrossRef]
12. Law-Chune, S.; Aouf, L.; Dalphinet, A.; Levier, B.; Drillet, Y.; Drevillon, M. WAVERYS: A CMEMS global wave reanalysis during the altimetry period. *Ocean Dyn.* **2021**, *71*, 357–378. [CrossRef]
13. GEBCO Compilation Group. *The GEBCO 2026 Grid: A Continuous Terrain Model of the Global Oceans and Land*; British Oceanographic Data Centre: Liverpool, UK, 2026.
14. Cornett, A.M. A global wave energy resource assessment. In Proceedings of the 18th International Offshore and Polar Engineering Conference (ISOPE), Vancouver, BC, Canada, 6–11 July 2008.
15. Falcão, A.F.O. Wave energy utilization: A review of the technologies. *Renew. Sustain. Energy Rev.* **2010**, *14*, 899–918. [CrossRef]
16. Silva, D.; Rusu, E.; Guedes Soares, C. Evaluation of various technologies for wave energy conversion in the Portuguese nearshore. *Energies* **2013**, *6*, 1344–1364. [CrossRef]
17. Henderson, R. Design, simulation, and testing of a novel hydraulic power take-off system for the Pelamis wave energy converter. *Renew. Energy* **2006**, *31*, 271–283. [CrossRef]
18. Weinstein, A.; Fredrikson, G.; Parks, M.J.; Nielsen, K. AquaBuOY—The offshore wave energy converter: Numerical modelling and optimization. In Proceedings of the MTS/IEEE OCEANS Conference, Kobe, Japan, 9–12 November 2004; pp. 1854–1859.
19. Kofoed, J.P.; Frigaard, P.; Friis-Madsen, E.; Sørensen, H.C. Prototype testing of the wave energy converter Wave Dragon. *Renew. Energy* **2006**, *31*, 181–189. [CrossRef]
20. Whittaker, T.; Folley, M. Nearshore oscillating wave surge converters and the development of Oyster. *Philos. Trans. R. Soc. A* **2012**, *370*, 345–364. [CrossRef] [PubMed]
21. Wave Star, A. *Wavestar Prototype at Roshage: Performance Data for ForskVE Project No. 2009-1-10305, Phase 1 & 2*; Wave Star A/S: Brøndby, Denmark, 2013.
22. Rusu, E.; Onea, F. Estimation of the wave energy conversion efficiency in the Atlantic Ocean close to the European islands. *Renew. Energy* **2016**, *85*, 687–703. [CrossRef]
23. Guillou, N.; Lavidas, G.; Chapalain, G. Wave energy resource assessment for exploitation: A review. *J. Mar. Sci. Eng.* **2020**, *8*, 705. [CrossRef]
24. Guo, B.; Ringwood, J.V. A review of wave energy technology from a research and commercial perspective. *IET Renew. Power Gener.* **2021**, *15*, 3065–3090. [CrossRef]
25. Todalshaug, J.H.; Ásgeirsson, G.S.; Hjálmarsson, E.; Maillet, J.; Möller, P.; Pires, P.; Guérinel, M.; Lopes, M. Tank testing of an inherently phase-controlled wave energy converter. *Int. J. Mar. Energy* **2016**, *15*, 68–84. [CrossRef]
26. Rafiee, A.; Fievez, J. Numerical prediction of extreme loads on the CETO wave energy converter. In Proceedings of the 11th European Wave and Tidal Energy Conference (EWTEC), Nantes, France, 6–11 September 2015.
27. Durap, A. From Black Box to Transparency: An Explainable Machine Learning (ML) Framework for Ocean Wave Prediction Using SHAP and Feature-Engineering-Derived Variable. *Mathematics* **2025**, *13*, 3962. [CrossRef]
28. Durap, A. Machine Learning-Based Wind Speed Prediction Using Random Forest: A Cross-Validated Analysis for Renewable Energy Applications. *Turk. J. Eng.* **2025**, *9*, 508–518. [CrossRef]
29. Durap, A. Explainable Machine Learning for Bathymetric Mapping: Adaptive Normalization and Feature Engineering in Complex Seabed Terrains. *Ocean Sci. J.* **2025**, *60*, 52. [CrossRef]

30. Bab, Y.; Kutlu, A. Mixed Finite Elements for Higher-order Laminated Cylindrical and Spherical Shells. *Turk. J. Civ. Eng.* **2025**, *36*, 51–74. [CrossRef]
31. Başakin, E.E.; Özger, M. Monthly River Discharge Prediction by Wavelet Fuzzy Time Series Method. *Int. J. Uncertain. Fuzziness Knowl.-Based Syst.* **2021**, *29*, 17–35. [CrossRef]